Letter

Vol. 48, No. 12 / 15 June 2023 / Optics Letters 3219

Optics Letters

High-spatial-resolution φ-OFDR shape sensor based on multicore optical fiber with femtosecond-laser-induced permanent scatter arrays

Cailing Fu,[1,2] Yanjie Meng,[1,2] Lin Chen,[1,2] Huajian Zhong,[1,2] Chao Du,[1,2] Jun He,[1,2] Xiaoyu Weng,[1] Liwei Liu,[1] Junle Qu,[1] and Yiping Wang[1,2,*]

[1]Key Laboratory of Optoelectronic Devices and Systems of Ministry of Education/GuangDong Province, College of Physics and Optoelectronic Engineering, Shenzhen University, Shenzhen 518060, China

[2]Shenzhen Key Laboratory of Photonic Devices and Sensing Systems for Internet of Things, Guangdong and Hong Kong Joint Research Centre for Optical Fibre Sensors, Shenzhen University, Shenzhen 518060, China

*ypwang@szu.edu.cn

Received 30 January 2023; revised 26 April 2023; accepted 26 April 2023; posted 26 April 2023; published 9 June 2023

An optical fiber φ-OFDR shape sensor with a submillimeter spatial resolution of 200 μm was demonstrated by using femtosecond-laser-induced permanent scatter array (PS array) multicore fiber (MCF). A PS array was successfully inscribed in each slightly twisted core of the 400-mm-long MCF. The two-dimensional (2D) and three-dimensional (3D) shapes of the PS-array-inscribed MCF were successfully reconstructed by using PS-assisted φ-OFDR, vector projections, and the Bishop frame based on the PS-array-inscribed MCF. The minimum reconstruction error per unit length of the 2D and 3D shape sensor was 2.21% and 1.45%, respectively.

https://doi.org/10.1364/OL.486644

Optical fiber shape sensing (OFSS), a proprioceptive type of sensing, has been widely used due to its advantages: electromagnetic immunity, a small size, and a light weight [1]. Currently, various techniques based on wavelength division multiplexing [2], Brillouin optical time domain analysis [3], Brillouin optical correlation domain analysis [4], phase-sensitive optical time domain reflectometry [5], and optical frequency domain reflectometry (OFDR) [6,7] have been proposed to achieve OFSS. Among them, shape sensing using OFDR is particularly promising due to its high measurement accuracy and spatial resolution. To improve the measurement accuracy, a UV-enhanced SMF cluster [8], an MgO-doped-SMF cluster [9], and multicore fiber (MCF) with a fiber Bragg grating array (FBG array) fabricated by a UV [10] or femtosecond [2] laser have been demonstrated. Compared with that inscribed by a UV laser, the femtosecond laser inscribed FBG array is more resistant to high temperatures [11]. In the case of low spatial resolution, an interpolation method is necessary to improve the accuracy and smoothness of shape reconstruction [12]. Point reflectors fabricated by a femtosecond laser have also been proposed to improve the spatial resolution for distributed acoustic sensing [13], hydrogen gas sensing [14], and high-temperature sensing [15]. The wavelength shift of the point reflectors under strain could be demodulated by using spectrum-based OFDR, but the sensing spatial resolution is limited by the number of samples in the sliding widow of the inverse fast Fourier transform (FFT). Compared with spectrum-based OFDR, no sliding window is applied to the spatial domain signal to conduct inverse FFT and cross correlation for φ-OFDR, which could exert its full potential in high resolution [16–18]. A strain sensor with submillimeter spatial resolution that used permanent-scatter-assisted φ-OFDR was also demonstrated [19].

In this Letter, a φ-OFDR shape sensor with a spatial resolution of 200 μm was demonstrated by using femtosecond-laser-induced permanent scatter array (PS array) MCF. A fabrication strategy was developed to inscribe PS arrays effectively and accurately into each slightly twisted core of the MCF. The two-dimensional (2D) and three-dimensional (3D)-shape-sensing properties of the obtained PS-array-inscribed MCF were investigated. Moreover, the detailed process of shape reconstruction by using PS-assisted φ-OFDR, vector projections, and the Bishop frame based on the PS-array-inscribed MCF was also studied. Furthermore, the 2D and 3D shape reconstruction errors were compared.

As shown in Fig. 1(a), a femtosecond laser micromachining system consisting of a shutter, half-wave plate (HWP), Glan-prism (GP) polarizer, and beam splitter (BS) was built to inscribe a permanent scatter array (PS array) in each core of commercial multicore optical fiber (MCF, YOFC). The nominal core/cladding diameter and the space between two cores of the MCF were 8/150 μm and 42 μm, respectively. The MCF included a central core, i.e., core 0, and six hexagonally arranged outer cores, i.e., core 1, core 2, core 3, core 4, core 5, and core 6, as shown in the inset of Fig. 1(b). A single pulse with an energy of 134.5 nJ was focused onto each core of the MCF through an 100× oil-immersion microscope objective. With the assistance of a charge-coupled device (CCD), the PS array in each core was inscribed by moving the MCF, which was installed on a high-precision three-axis translation stage with two optical fiber holder clamps on the right and left. Note that the MCF was firstly leveled by adjusting the three-axis translation stage to ensure that the positions of the inscribed PSs in the cores were in the same cross section.

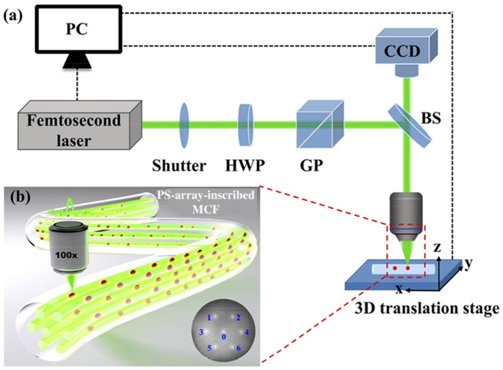

Fig. 1. (a) Schematic diagram of the femtosecond laser fabrication setup for inscribing permanent scatters in multicore optical fiber (MCF). HWP: half-wave plate, GP: Glan-prism polarizer, BS: beam splitter. (b) Schematic diagram of multicore fiber with permanent scatters.

Although commercial MCF has a nominal parameter, a torsion of 0.029 rad/mm and an outer core space fluctuation of 39.5 to 42.5 µm are observed during the process of moving the MCF. To inscribe the PS array effectively and accurately into each slightly twisted core, a fabrication strategy was developed. The detailed fabrication process of the PS array in each core is listed as follows.

Step 1: Find the central core, i.e., core0, of the MCF fixed on the right fiber clamp, focus the femtosecond laser onto the upper edge of the fiber cladding, and then move 75 µm along the z axis, i.e., along the cladding radius to the center core. At this time, the coordinate is recorded as (x_0, y_0, z_0).

Step 2: Find any outer core in the same cross section and record the coordinate as (x_R, y_R, z_R). Then, the coordinates of the other five outer cores, i.e., (y_i, z_i), can be calculated by

$$\begin{bmatrix} y_i \\ z_i \end{bmatrix} = \begin{bmatrix} \cos\alpha & -\sin\alpha \\ \sin\alpha & \cos\alpha \end{bmatrix} * \begin{bmatrix} y_R - y_0 \\ z_R - z_0 \end{bmatrix} + \begin{bmatrix} y_0 \\ z_0 \end{bmatrix}, \tag{1}$$

where α is changed from 60° to 120°, 180°, 240°, and 300° until all outer cores are positioned.

Step 3: Move the three-axis translation stage along the x axis to the left fiber clamp, and then repeat step 2 until all seven cores are found. It is worth mentioning that the known right outer core should be the same outer core on the left. In this way, the core coordinates on the right and left can be obtained, i.e., (x_R, y_R, z_R) and (x_L, y_L, z_L), respectively. Since the center core is a straight line, we can interpolate any inscribed position according to the predefined PS interval. In addition, the inevitable slight torsion induced by clamping the MCF on the fiber holder makes the outer core twist. Fortunately, this twist angle can be calculated and compensated for using the obtained left and right coordinates. Then the specific position of the PS can be generated by calculation, and the PS can be inscribed by moving the translation stage to the calculated position.

Step4: Use the winding system to move to the next fiber section, as reported in Ref. [11].

In this way, a 400-mm-long PS-array-inscribed MCF with 13,965 PSs was obtained by repeating steps 1–3, where the interval between two PSs was 200 µm, as illustrated in Fig. 1(b).

To measure the Rayleigh backscattering (RBS) amplitude of each core for the PS-array-inscribed MCF, traditional optical frequency domain reflectometry (OFDR) was employed, as illustrated in Fig. 2(a). Note that the MCF was spliced with by a

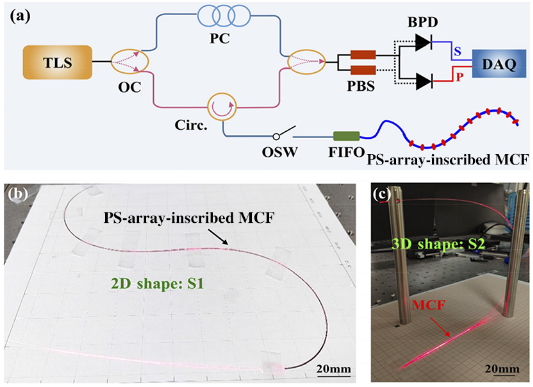

Fig. 2. (a) Schematic diagram of the optical frequency domain reflectometry (OFDR) shape sensor based on MCF with femtosecond-laser-induced PS arrays. Schematic diagrams of (b) 2D and (c) 3D shape sensing by using a 400-mm-long PS-array-inscribed MCF with 13,965 PSs. Note that the black S-curve in Fig. 2(b) was printed on A4 paper.

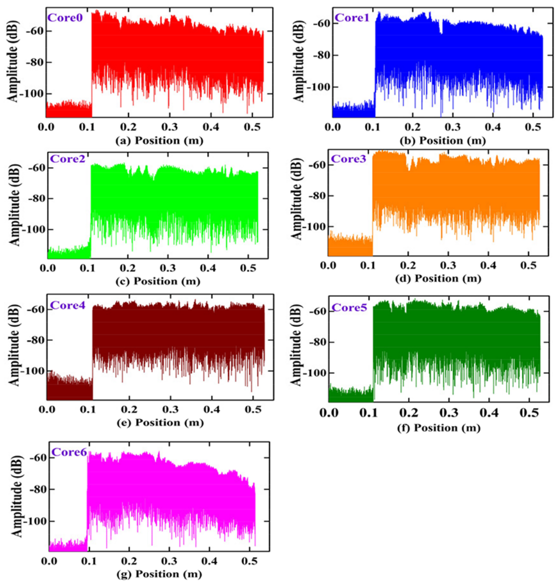

Fig. 3. Measured Rayleigh backscattering (RBS) amplitudes of (a) core 0, (b) core 1, (c) core 2, (d) core 3, (e) core 4, (f) core 5 and (g) core 6, respectively, for the PS-array-inscribed MCF.

fan-in/out (FIFO), and a 1×8 mechanical optical switch (OSW) was used to switch the light to each core. The wavelength of the tunable laser source (TLS) was swept from 1540.0 to 1564.7 nm with a sweep rate of 100 nm/s. As shown in Fig. 3, the RBS of each core was enhanced by the PS array. However, the amplitudes of the PSs in the same core are not completely equal, and the average amplitudes of the cores are also different. One reason for this is that the focus of the femtosecond laser deviated from the center of the fiber core, which lowered the RBS amplitude of the PS array. Another reason is that the femtosecond laser was not perfectly perpendicular to the fiber surface, especially for the outer core. In this case, the focus of the laser would have diverged slightly due to the existence of the fiber, i.e., the cylindrical lens phenomenon.

To verify the performance of the PS-array-inscribed MCF, the 2D- and 3D-shape-sensing properties were investigated. As

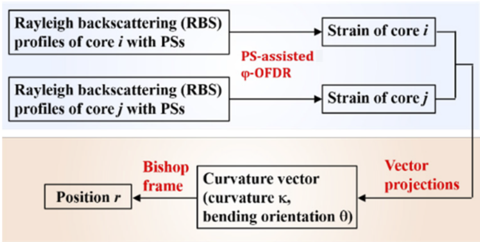

Fig. 4. Flow chart for shape reconstruction using φ-OFDR and the PS-array-inscribed MCF.

shown in Figs. 2(b) and 2(c), the PS-array-inscribed MCF was bent into a designed S-curve and an arbitrary three-dimensional shape, which were denoted as S1 and S2, respectively. To minimize the introduction of torsion during MCF placement, the fiber should be kept as close to the plate as possible instead of lifting, lowering, and bending the fiber during 2D-shape sensing. For 3D-shape sensing, external forces introduced by contact with the fiber should be avoided. The process of shape reconstruction using φ-OFDR and PS-array-inscribed MCF is illustrated in Fig. 4. Firstly, the strain distribution of each core was demodulated by extracting the phase difference of the PS array, i.e., using the PS-assisted φ-OFDR method in Ref. [18]. Secondly, the curvature vector, including the curvature, i.e., κ, and the bending orientation, i.e., θ, was obtained from two outer cores by using the vector projections method in Ref. [20]. Finally, the 2D and 3D shapes were reconstructed using the Bishop frame [21], which can be expressed as

$$\frac{d}{ds}\begin{bmatrix}\boldsymbol{T}\\ \boldsymbol{M}_1\\ \boldsymbol{M}_2\end{bmatrix}=\begin{bmatrix}0 & k_1 & k_2\\ -k_1 & 0 & 0\\ -k_2 & 0 & 0\end{bmatrix}\cdot\begin{bmatrix}\boldsymbol{T}\\ \boldsymbol{M}_1\\ \boldsymbol{M}_2\end{bmatrix}, \tag{2}$$

where $\boldsymbol{T}$ is the tangent vector, and $\boldsymbol{M_1}$ and $\boldsymbol{M_2}$ are two normal vectors perpendicular to $\boldsymbol{T}$. k_1 and k_2 can be expressed as

$$k_1 = \kappa * \cos(\theta), \tag{3}$$

$$k_2 = \kappa * \sin(\theta). \tag{4}$$

The space position of each PS, i.e., $\boldsymbol{r}(s)$, can be obtained using the tangent vector, i.e., $\boldsymbol{T}$, by

$$\mathbf{r}(s) = \sum_{i=0}^{N} \boldsymbol{T}(i)\cdot\Delta s, \tag{5}$$

where Δs is the spatial resolution of the PSs-assisted φ-OFDR, i.e., the interval between two PSs, corresponding to $\Delta s = 200$ µm. N is the number of PSs in each core, and s is the length of the PS-array-inscribed MCF, i.e., 400 mm.

As shown in Fig. 2(b), a designed S-curve was printed beforehand on paper, and then the PS-array-inscribed MCF was placed and fixed with tape along the designed S-curve, i.e., S1. The arc length of S1 was 400 mm, corresponding to the length of the PS-array-inscribed MCF. The curvature was gradually changed from 0 to 25 m^{-1}, and the bending orientation was suddenly changed by 180° in the middle of the arc. The strain distribution of each core for the PS-array-inscribed MCF is illustrated in Fig. 5(a). The recovered strain profiles are not theoretical sine curves due to a slight torsion of 0.029 rad/mm of the employed commercial MCF outer core. The curvature, i.e., κ, and the bending orientation, i.e., θ, were obtained from the combination

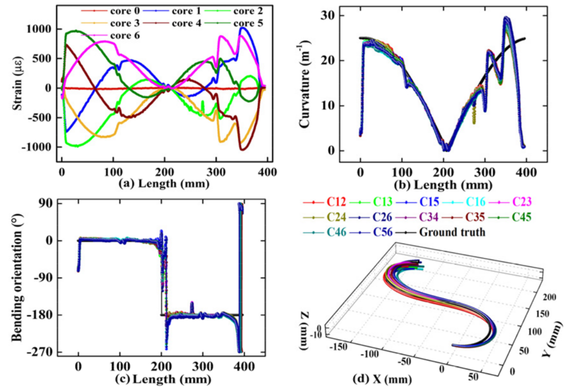

Fig. 5. (a) Obtained strain distribution of each core for the PS-array-inscribed MCF, based on PS-assisted φ-OFDR, when the MCF was placed along the designed 2D S-curve, i.e., S1. (b) Calculated curvature and (c) bending orientation of the PS-array-inscribed MCF from combining two outer cores using the vector projections method. (d) 2D shape reconstructed using two outer cores in combination based on the Bishop frame. Note that Cij is the combination of core i and core j (e.g., C12 is the combination of core 1 and core 2).

Table 1. Shape Reconstruction Errors of Pairs of Outer Cores

Cores	C12	C13	C15	C16	C23	C24	C26
S1 (%)	2.73	2.64	2.72	3.97	2.21	2.50	2.32
S2 (%)	3.68	4.30	4.56	3.00	3.13	3.83	1.45
Cores	C34	C35	C45	C46	C56	Integration	
S1 (%)	2.70	2.65	2.63	4.03	3.08	**2.01**	
S2 (%)	3.34	4.42	3.87	2.05	2.30	**1.25**	

of two outer cores, i.e., C12, C13, C15, C16, C23, C24, C25, C34, C35, C45, C46, and C56 (here, Cij is the combination of core i and core j; e.g., C12 is the combination of core 1 and core 2) by using the vector projections method, as shown in Figs. 5(b) and 5(c). As shown in Fig. 5(d), the reconstructed 2D shape was in good agreement with the designed S-curve, i.e., S1, when using the three vectors, i.e., T, M_1, and M_2, in the Bishop frame. Note that no interpolation method was used for fiber shape reconstruction due to its high spatial resolution, i.e., 200 µm. Moreover, the sudden 180° change in the bending orientation was also well recovered. This indicates that both the continuous and disjunctive changes in the curvature vector for the PS-array-inscribed MCF were well recognized by using the Bishop frame instead of the Frenet–Serret frame. The deviations in some positions were induced by a tiny misalignment between the designed S-curve and the actual curve pasted with tape. As listed in Table 1, the reconstruction error per unit length of the two different outer core combinations for S1 varied from 2.21% to 4.03%.

Moreover, the 3D-shape-sensing property of the PS-array-inscribed MCF was also further investigated. As shown in Fig. 6, the reconstructed 3D shape was also in good agreement with the designed curve, i.e., S2. This further indicated that the 2D and 3D shapes could be well reconstructed by using the PS-array-inscribed MCF. The minimum and maximum reconstruction errors of C26 and C35 for S2 were 1.45% and 4.42%, respectively, as listed in Table 1. Note that the reconstruction error is defined as the error at the end position, where the actual end

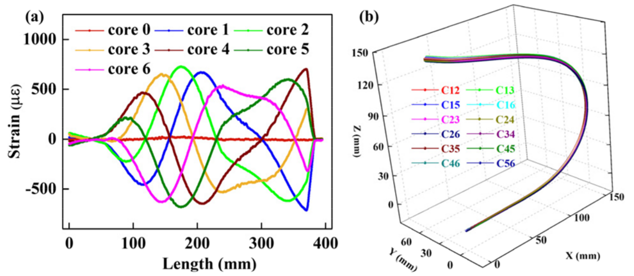

Fig. 6. (a) Obtained strain distribution of each core for the PS-array-inscribed MCF, based on PS-assisted φ-OFDR, when the MCF was bent into an arbitrary 3D shape. (b) 3D curves reconstructed using two outer cores in combination based on the Bishop frame.

Table 2. Comparison between the Previous Research and the Proposed Method

Work	Sensing fiber	Spatial resolution
[6]	MCF grating arrays	10.0 mm
[7]	Plane MCF	3.6 mm
[8]	UV-enhanced-SMF cluster	10.0 mm
[9]	MgO-doped-SMF cluster	5.0 mm
This work	MCF with PS arrays	0.2 mm

position could be accurately measured by a ruler. It could be seen that the minimum reconstruction errors of S1 and S2 were not from the same core combination. The reason for this is that the reconstruction error is dependent not only on the strain accuracy but also the fiber shape complexity [22]. As indicated in Table 1, the shape reconstruction errors of S1 and S2 were reduced to 2.01% and 1.25%, respectively, by using the integration method in Ref. [20]. This method could be used to improve the accuracy of the reconstructed shape by integrating the obtained fiber shapes from all core combinations. In addition, the proposed shape sensor exhibited higher spatial resolution, i.e., 0.2 mm, as presented in Table 2.

In conclusion, a φ-OFDR 2D and 3D shape sensor with a spatial resolution of 200 μm was demonstrated by using femtosecond-laser-induced PS-array MCF. The PS array was successfully inscribed in each slightly twisted core of the 400-mm-long MCF. The strain distribution of each core was demodulated by extracting the phase difference of the PS array, i.e., PS-assisted φ-OFDR, while the curvature vector was calculated by the vector projections method. Using the Bishop frame, delicate and smooth 2D and 3D shapes of the PS-array-inscribed MCF were accurately reconstructed with the highest spatial resolution, i.e., 200 μm. The reconstruction error per unit length of the 2D and 3D shape sensors was 2.21% and 1.45%, which could be further reduced to 2.01% and 1.25%, respectively.

Funding. National Key Research and Development Program of China (SQ2021YFE010025); National Natural Science Foundation of China (U1913212); Natural Science Foundation of Guangdong Province (2019B1515120042, 2021A1515011925); Science and Technology Innovation Commission of Shenzhen (20200810121618001, JCYJ20200109114020865, JCYJ20200109114201731, JSGG20201102152200001); Shenzhen Key Laboratory of Photonic Devices and Sensing Systems for Internet of Things.

Disclosures. The authors declare no conflicts of interest.

Data availability. Data underlying the results presented in this paper are not publicly available at this time but may be obtained from the authors upon reasonable request.

REFERENCES

1. I. Floris, J. M. Adam, P. A. Calderon, and S. Sales, Opt. Laser Eng. **139**, 106508 (2021).
2. A. Wolf, A. Dostovalov, K. Bronnikov, and S. Babin, Opt. Express **27**, 13978 (2019).
3. Z. Y. Zhao, M. A. Soto, M. Tang, and L. Thevenaz, Opt. Express **24**, 25211 (2016).
4. M. Jang, J. H. Choi, J. S. Kim, Y. W. Song, K. Y. Song, and J. Kim, IEEE J. Select. Topics Quantum Electron. **26**, 1 (2020).
5. L. Szostkiewicz, M. A. Soto, Z. S. Yang, A. Dominguez-Lopez, I. Parola, K. Markiewicz, A. Pytel, A. Kolakowska, M. Napierala, T. Nasilowski, and L. Thevenaz, Opt. Express **27**, 20763 (2019).
6. J. P. Moore and M. D. Rogge, Opt. Express **20**, 2967 (2012).
7. Z. Chen, C. H. Wang, Z. Y. Ding, D. F. Zhu, H. H. Guo, M. Pan, Y. Yu, K. Liu, J. F. Jiang, and T. G. Liu, IEEE Photonics J. **13**, 1 (2021).
8. F. Parent, S. Loranger, K. K. Mandal, V. L. Iezzi, J. Lapointe, J. S. Boisvert, M. D. Baiad, S. Kadoury, and R. Kashyap, Biomed. Opt. Express **8**, 2210 (2017).
9. A. Beisenova, A. Issatayeva, I. Iordachita, W. Blanc, C. Molardi, and D. Tosi, Opt. Express **27**, 22074 (2019).
10. P. S. Westbrook, T. Kremp, K. S. Feder, W. Ko, E. M. Monberg, H. C. Wu, D. A. Simoff, T. F. Taunay, and R. M. Ortiz, J. Lightwave Technol. **35**, 1248 (2017).
11. B. J. Xu, J. He, B. Du, X. Z. Xiao, X. Z. Xu, C. L. Fu, J. He, C. R. Liao, and Y. P. Wang, Opt. Express **29**, 32615 (2021).
12. S. Jaeckle, T. Eixmann, H. Schulz-Hildebrandt, G. Huettmann, and T. Paetz, Int J CARS **14**, 2137 (2019).
13. B. Redding, M. J. Murray, A. Donko, M. Beresna, A. Masoudi, and G. Brambilla, Opt. Express **28**, 14638 (2020).
14. R. T. Cao, Y. Yang, M. H. Wang, X. R. Yi, J. Y. Wu, S. Huang, and K. P. Chen, Opt. Lett. **45**, 3163 (2020).
15. B. Du, J. He, B. J. Xu, X. Z. Xu, C. L. Fu, P. F. Li, X. Z. Xiao, S. Liu, Y. T. Yang, and Y. P. Wang, J. Lightwave Technol. **40**, 7447 (2022).
16. D. K. Gifford, M. E. Froggatt, and S. T. Kreger, *21st International Conference on Optical Fiber Sensors* 7753 (2011).
17. S. Y. Zhao, J. W. Cui, Z. J. Wu, Z. Y. Wang, and J. B. Tan, J. Lightwave Technol. **39**, 4101 (2021).
18. C. H. Wang, K. Liu, Z. Y. Ding, J. F. Jiang, Z. E. Chen, Y. F. Feng, Y. Y. Zheng, Q. Q. Liu, and T. G. Liu, J. Lightwave Technol. **38**, 5825 (2020).
19. Y. Meng, C. Fu, L. Chen, C. Du, H. Zhong, Y. Wang, J. He, and W. Bao, Opt. Lett. **47**, 6289 (2022).
20. Y. J. Meng, C. L. Fu, C. Du, L. Chen, H. J. Zhong, P. F. Li, B. J. Xu, B. Du, J. He, and Y. P. Wang, J. Lightwave Technol. **39**, 6624 (2021).
21. J. W. Cui, S. Y. Zhao, C. Q. Yang, and J. B. Tan, IEEE Photonics J. **10**, 1 (2018).
22. S. Li, P. D. Hua, Z. Y. Ding, K. Liu, Y. Yang, J. P. Zhao, M. Pan, H. H. Guo, T. Zhang, L. Liu, J. F. Jiang, and T. G. Liu, Opt. Express **30**, 43255 (2022).